Available online at www.sciencedirect.com

ScienceDirect

Advances in Space Research 76 (2025) 4747–4764

ADVANCES IN SPACE RESEARCH (a COSPAR publication)

www.elsevier.com/locate/asr

Seismic interferometry with mobile spaceborne platforms

Nicholas Dorogy [a,*], Paul Sava [a], Erik Asphaug [b]

[a] Center for Wave Phenomena, Department of Geophysics, Colorado School of Mines, 1500 Illinois Street, Golden, CO 80401, USA
[b] Lunar and Planetary Laboratory, University of Arizona, 1629 E University Blvd, Tucson, AZ 85721, USA

Received 18 October 2024; received in revised form 22 May 2025; accepted 7 July 2025
Available online 17 July 2025

Abstract

Understanding the deep interior structure of small planetary bodies is crucial for improving planetary formation and evolution theories, deflecting potentially hazardous near-Earth objects, and mapping the distribution of resources vital for sustained human exploration (e.g., water ice). Radar is a commonly-used remote exploration tool, but scattering and attenuation effects can limit its depth of penetration to the near subsurface. Seismic acquisition, however, is well suited to study deep interior structure, although landing seismic instrumentation on a planet or small body is complex and risky. To acquire seismic data remotely, we can use remote sensing seismometers that measure surface motion with laser Doppler vibrometers (LDVs). In lieu of active sources (kinetic impactors and explosives) which could eject debris that are hazardous for spacecraft operation, naturally occurring seismic activity can be used to recover travel times according to the theory of seismic interferometry. However, orbiter-mounted LDVs are mobile and thus sample different points on the ground unlike conventional seismometers that observe a fixed point. In this paper, we adapt the theory of seismic interferometry to account for receiver motion using asteroid 99942 Apophis as a test demonstration. We use artificially stimulated internal sources to mimic natural seismicity thus enabling acquisition with the remote sensing seismometer configuration. This technique provides the ability to remotely collect seismic data without the risks associated with landed instruments and active seismic sources.
© 2025 The Author(s). Published by Elsevier B.V. on behalf of COSPAR. This is an open access article under the CC BY-NC-ND license (http://creativecommons.org/licenses/by-nc-nd/4.0/).

Keywords: Interferometry; Asteroid; Seismic; Ambient; Vibrometry

1. Introduction

1.1. Small body exploration

Small body interiors are thus far restricted to inferences (Asphaug et al., 2002; Binzel et al., 2003; Asphaug, 2004; Michel et al., 2015) and their direct observation awaits future spacecraft mission studies using electromagnetic (Herique et al., 2018a) or seismic (Murdoch et al., 2017; Sava and Asphaug, 2019; DellaGiustina et al., 2024) techniques. There are several major reasons, both scientific and pragmatic, for why an understanding of small body interiors is so important.

First, small bodies are the primary source of meteorites (Greenwood et al., 2020), which derive either from the surfaces or interiors of small bodies depending on impact physics. Meteorites, in turn, represent the vast majority of what we know of the composition of the objects that formed the planets. Thus, making a quantitative asteroid-meteorite connection is paramount and depends on the mechanical properties of their surfaces and interiors.

Second, the mechanics of small bodies governs their collision and disruption physics: How friable are they? How compactible? Knowing these, we can infer the size distribution of their disruption fragments, as well as their associated fragment ejection velocity. These connect directly to the delivery of meteorites, and also to the origin of asteroid families (almost every asteroid today being a fragment of a disrupted parent body) (Marzari et al., 1995; Michel et al.,

* Corresponding author.
E-mail address: ndorogy@mines.edu (N. Dorogy).

https://doi.org/10.1016/j.asr.2025.07.020
0273-1177/© 2025 The Author(s). Published by Elsevier B.V. on behalf of COSPAR.
This is an open access article under the CC BY-NC-ND license (http://creativecommons.org/licenses/by-nc-nd/4.0/).

2003). Furthermore, the mechanics of small bodies directly connects to the physics of primordial body accretion, namely, the velocity at which bodies grow larger through mechanical dissipation, versus at which speed they disrupt.

Third, knowledge of interiors allows us to interpret a small body's bombardment history and the record of cratering at their surface (Richardson et al., 2005; Murdoch et al., 2017; Asphaug, 2008). This in turn is significant for understanding solar-system evolutionary history, including in the outer solar system where most of what we can learn is through fast flybys (Spencer et al., 2020) and interpretation of the formation and dynamical ages of asteroids (Walsh et al., 2019).

Fourth, the mechanisms of asteroid deflection and disruption that are envisioned for mitigating hazardous small bodies are very sensitive to their subsurface properties and the transmission of stress wave energy throughout their interiors (Asphaug, 2004; Raducan et al., 2024). Bodies that are crushable and weak, for example, may be able to absorb greater impact energy without disrupting into equally-hazardous pieces, while solid brittle objects might fragment into dangerous subcomponents. Modeling these events requires not only impact experiments like DART, but also the ability to model deflections based on different parameters (Stickle et al., 2022) that can be obtained from seismic studies.

Lastly, near-Earth asteroids are desired for their potential resources, including water–ice (for in *in situ* applications like propulsion and human sustainment), as well as for precious metals. As is true of any mining operation, access to these materials relies upon a basic geophysical understanding of their material properties (as can be derived from seismology) and an assessment of resource density and distribution (as can be obtained from wave-based imaging).

1.2. Remote sensing seismology

Exploration of small planetary bodies (asteroids, comets, small moons) is extremely valuable for understanding the formation and evolution of our solar system (Brownlee and Joswiak, 2017; Pieters and Mcfadden, 2003; Herique et al., 2018b). The interior structure of these bodies can provide insight into early solar-system formation, the coalescence and evolution of planetary bodies, and the distribution of resources (especially water–ice) in our solar system (Minton and Malhotra, 2010; Day, 2016; Asphaug, 2009). Moreover, understanding the interior composition and structure of these bodies is critical for planetary defense strategies as it enables us to predict their behavior under external forces (i.e., redirection or deflection missions) (Satpathy et al., 2022).

Optical observations are well suited for studying the surface of these bodies, but provide little to no information about the interior structure (DellaGiustina et al., 2019; Marchis et al., 2006). Radar imaging is commonly used to study the near subsurface by measuring alterations in the electrical properties of the underlying materials, but rocky conglomerations create significant signal attenuation that can limit the depth of penetration to within several wavelengths (Pettinelli et al., 2022). This is particularly problematic for rubble pile asteroids like 101955 Bennu (Barnouin et al., 2019). Seismic wave propagation, however, is sensitive to mechanical changes of the subsurface and is not limited by the presence of rubble pile structures. Furthermore, penetration depths can reach several kilometers making it an ideal tool for studying both the deep and shallow interior structure of small planetary bodies. For some radar-penetrable bodies like comets, an opportunistic combination of seismic and radar investigation can provide cross-validation and combined insights, similar to the synergistic use of gravitational and seismic experiments to determine interior mass distributions.

Traditional seismometers rely on coupling with the ground to measure seismic activity, an extremely challenging task in microgravity environments made more difficult by potentially complex surface conditions unknown prior to arrival. Moreover, surface waves can uplift implanted receivers causing them to lose contact with the ground and miss critical seismic events. Microgravity conditions drastically increase the time it takes for these receivers to resettle after being uplifted, thus reducing observation time (Murdoch et al., 2017). An alternative acquisition system uses laser Doppler vibrometers (LDVs) to measure seismic activity (Sava and Asphaug, 2019). LDVs use a known reference laser and measurements of the Doppler shift of the same beam reflected off a surface to deduce the velocity at which the surface is moving (Rothberg et al., 2017). Wavelengths returning to the sensor that are longer than the original reference wavelength indicate that the surface is moving away from the sensor, while wavelengths shorter than the reference indicate that the surface is moving towards the sensor. These observations allow us to record seismic activity exactly as a traditional geophone might (Clinton and Heaton, 2002). Although LDVs are commonly depicted with a single reference laser, array LDVs are also available that create a grid of laser spots each with its own unique Doppler shift (Fu et al., 2011). Multiple observation points enables us to record seismic activity with the receiver arrays desired for angle-of-arrival filtering. Since LDVs do not require physical contact with the surface, they are ideal for use on spacecraft in orbit. It is through the spacecrafts' orbit that we cause the receivers to be in motion, thus requiring the use of local cross-correlation as described in Section 2.

Moreover, by introducing two LDVs orbiting on opposite sides of the body, we can perform ambient seismic interferometry using naturally occurring seismic sources. These sources can be generated by a variety of processes on small planetary bodies such as tidal deformations, micro-meteorite impacts, Yarkovsky–O'Keefe–Radzievskii–Paddack (YORP) effect, unstable rock piles, and thermally induced cracking (DellaGiustina et al., 2024; Asphaug, 2008; Graves et al., 2018; Nishiyama et al.,

2021; Graves et al., 2019; Molaro et al., 2020a; Molaro et al., 2020b). With this acquisition geometry, we can record ambient seismic activity from orbiting spacecraft to estimate the travel time between two points on the surface. Orbiting the target also lets the LDVs collect data at dense spatial intervals and from many illumination angles. Advanced seismic data-analysis techniques can then be used to produce high-resolution seismic images of the target's interior that are valuable for constraining the subsurface structure (Sava and Fomel, 2003).

1.3. Passive seismic acquisition

Seismic interferometry is a method used to infer subsurface properties by analyzing the interference of seismic waves observed at one (via auto-correlation) or more (via cross-correlation) independent receivers as first proposed by Claerbout (1968). Under certain assumptions discussed in Section 2, analysis of these interference patterns enable us to estimate the travel time between receivers. We may then use the recovered travel times to perform seismic imaging or inversion and subsequently produce a model of the subsurface (Zelt and Smith, 1992; Hole, 1992). The generalized interferometry method is common to a broad spectrum of sciences where it can be used to determine the travel time, medium velocity, or distance between points (Girard et al., 2023; Rosen et al., 2000; Acciari et al., 2019). For example, ocean-bottom surface waves can be used to estimate the travel time between seismic receivers on the ocean floor (Girard et al., 2023), interference patterns between synthetic aperture radar images can be used to determine surface displacement and displacement rate (Rosen et al., 2000), and modern imaging telescopes configured as optical intensity interferometers can be used to measure the angular diameter of stars (Acciari et al., 2019).

Seismic interferometry is more easily explained in the fundamental case where we can assume a 1D homogenous and lossless medium with two receivers at locations x_A and x_B as shown in Fig. 1(a). A source, located at x_S, emits an impulse at $t = 0$ propagating at the medium velocity c. At time $t_A = \frac{x_A - x_S}{c}$, the impulse is recorded by the receiver at x_A (Fig. 1(b)). We can represent the receiver's response to this impulse by the Green's function $G(x_A, x_S, t)$. In this notation, the first argument is the receiver location, the second argument is the source location, and the third argument is the time. After passing through receiver A, the impulse continues propagating to receiver B where it arrives at a later time $t_B = \frac{x_B - x_S}{c}$ (Fig. 1(c)). This signal is represented by $G(x_B, x_S, t)$. Seismic interferometry is the process of comparing, by cross-correlation, convolution, or deconvolution, signals observed at these two receivers to isolate the travel time, $\Delta t = t_B - t_A = \frac{x_B - x_A}{c}$, between them. The result of this cross correlation is illustrated in Fig. 1(d).

A corollary of the cross-correlation method is that the source location and propagation velocity do not need to be known to infer the propagation time between the separate receivers (Wapenaar et al., 2010). Consider again a wave that arrives first at receiver A and later at receiver B. The cross-correlation between the data observed at these receivers attempts to find an appropriate shift such that the data of receiver A matches the data of receiver B. Because receivers record data as a function of time, the amount of shift required to find the best match corresponds to the tra-

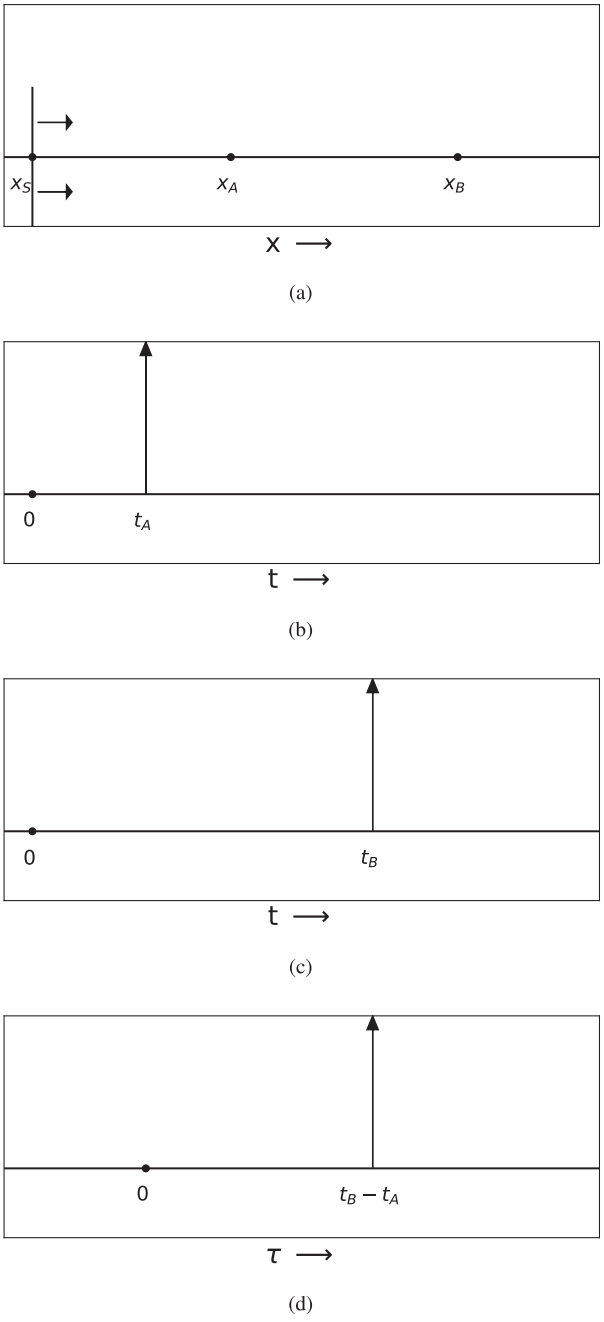


Fig. 1. 1D seismic interferometry example with stationary receivers adapted from Wapenaar et al. (2010). (a) A plane wave emitted at $t = 0$ from a source at location x_S. (b) The response recorded by the receiver at position x_A. (c) The response recorded by the receiver at position x_B. (d) The cross-correlation of the receiver responses in (b) and (c) forming an event at the travel time difference $t_B - t_A$.

vel time between the two receivers, $\Delta t = t_B - t_A$. By isolating the travel time between receivers A and B, cross-correlation effectively forms an experiment with a "virtual source" at the location of receiver A (Mehta et al., 2008).

Traditional implementations of seismic interferometry are applicable only when the receivers at x_A and x_B are stationary (Wapenaar et al., 2019). In this paper, we focus on the estimation of travel time between two or more *mobile* receivers which allows us to use seismometers on moving platforms such as drones or satellites (Sava and Asphaug, 2019). Potential future applications may also include ocean-floating seismometers and airborne seismic sounders on planetary bodies.

We first review the core assumptions of seismic interferometry with stationary receivers and provide a theoretical framework and accompanying computational examples for seismic interferometry with mobile receivers. We then illustrate this method with remote sensing seismology of small planetary bodies as a practical application that relies on mobile receivers.

2. Theory

Seismic interferometry relies on the use of cross-correlations (or alternatives like convolution and deconvolution) to estimate the travel time between separate receivers. We define the cross-correlation operation as

$$c(\tau) = \int_0^t u_A(t-\tau/2)u_B(t+\tau/2)dt, \tag{1}$$

where τ represents the time lag between the signal recordings, $u_A(t)$ and $u_B(t)$. Here, $u_A(t) = G(x_A, x_S, t)$ is the response recorded by receiver A and $u_B(t) = G(x_B, x_S, t)$ is the response recorded by receiver B. If we apply a Gaussian window to the data, we can localize the cross-correlation to a specific time $t = \gamma$ and obtain the subsequent local cross-correlation

$$c(\gamma;\tau) = \int_0^t u_A(t-\tau/2)u_B(t+\tau/2)g(\gamma-t;\tau)dt. \tag{2}$$

In this expression, g is a Gaussian window centered at γ that is applied to both signals $u_A(t)$ and $u_B(t)$. By integrating Eq. 2 over $g(\gamma - t;\tau)$, we create the computationally optimized local cross-correlation scheme defined by Hale (2006) and derived in Appendix A where

$$c(\tau) = \int_0^\gamma \int_0^t u_A(t-\tau/2)u_B(t+\tau/2)g(\gamma-t;\tau)dtd\gamma. \tag{3}$$

The width of this Gaussian window $g(\gamma - t;\tau)$ must be larger than the anticipated time shift between signals to ensure an accurate cross-correlation. The windowed data are cross-correlated to obtain local cross-correlations that are each centered at the sample γ. This process is repeated by recentering the Gaussian window at every time in the data set. By including integration over γ, Eq. 3 becomes equivalent to Eq. 1 creating a single cross-correlation over the duration of observation and all windowed data. Fig. 2(a) - (d) shows the effect of time-windowing the data on the cross-correlation. Although the added benefit of local cross-correlations is not immediately evident, we will see that this method is necessary when we consider mobile receivers.

Until now, we have focused on impulsive sources. However, this need not be the case. Consider an arbitrary waveform $s(t)$ propagating along the path from x_A to x_B. The response recorded at x_A is $u_A(t) = G(x_A, x_S, t) * s(t)$ and the response recorded at x_B is $u_B(t) = G(x_B, x_S, t) * s(t)$. Here, the Green's functions are convolved with the arbitrary source waveform $s(t)$ to provide the receiver response. The source waveform need not be known ahead of time allowing us to instead use *any* signal propagating between the receivers, including random ambient noise (Wapenaar et al., 2010). We can represent a more generalized local cross-correlation that incorporates arbitrary waveforms using the slightly modified result

$$c(\tau) = \int_0^\gamma \int_0^t S(t)u_A(t-\tau/2)u_B(t+\tau/2)g(\gamma-t;\tau)dtd\gamma, \tag{4}$$

where $S(t)$ is the autocorrelation of the (possibly unknown and random) source function. Wapenaar et al. (2010) provide a detailed treatment of this derivation for continuous signals in addition to a derivation for multi-dimensional cross-correlations that are required for 2D and 3D acquisition geometries.

The cross-correlations relied on by seismic interferometry are built upon several key assumptions. We first assume that receivers remain stationary over their duration of observation. Second, we require that noise sources be isotropically distributed around our receivers to ensure constructive interference at the correct travel time. Third, each source should be activated independently with an interval period that allows the wave to reach both receivers before another source is activated. Fourth, sources and receivers lie in an unbounded system without free surfaces (i.e., the system is open). Finally, we assume that the medium in which the wave travels is lossless (or nearly lossless). These assumptions are necessary to ensure that the cross-correlation of the receiver responses isolates the accurate travel time between the receivers. In the subsequent sections, we provide methods to relax these assumptions when such idealized conditions do not exist.

2.1. Stationary interferometry

Fig. 3(a) displays a simple source-receiver geometry in a constant velocity medium. In this example, every source is activated independently as a function of azimuthal angle ϕ and the receiver responses for each activation are cross-correlated to produce the correlation gather according to Wapenaar et al. (2010) and shown in Fig. 3(b). The travel time between A and B varies as a function of source angle ϕ. For a source located near $\phi = 90°$ or $\phi = 270°$, we sam-

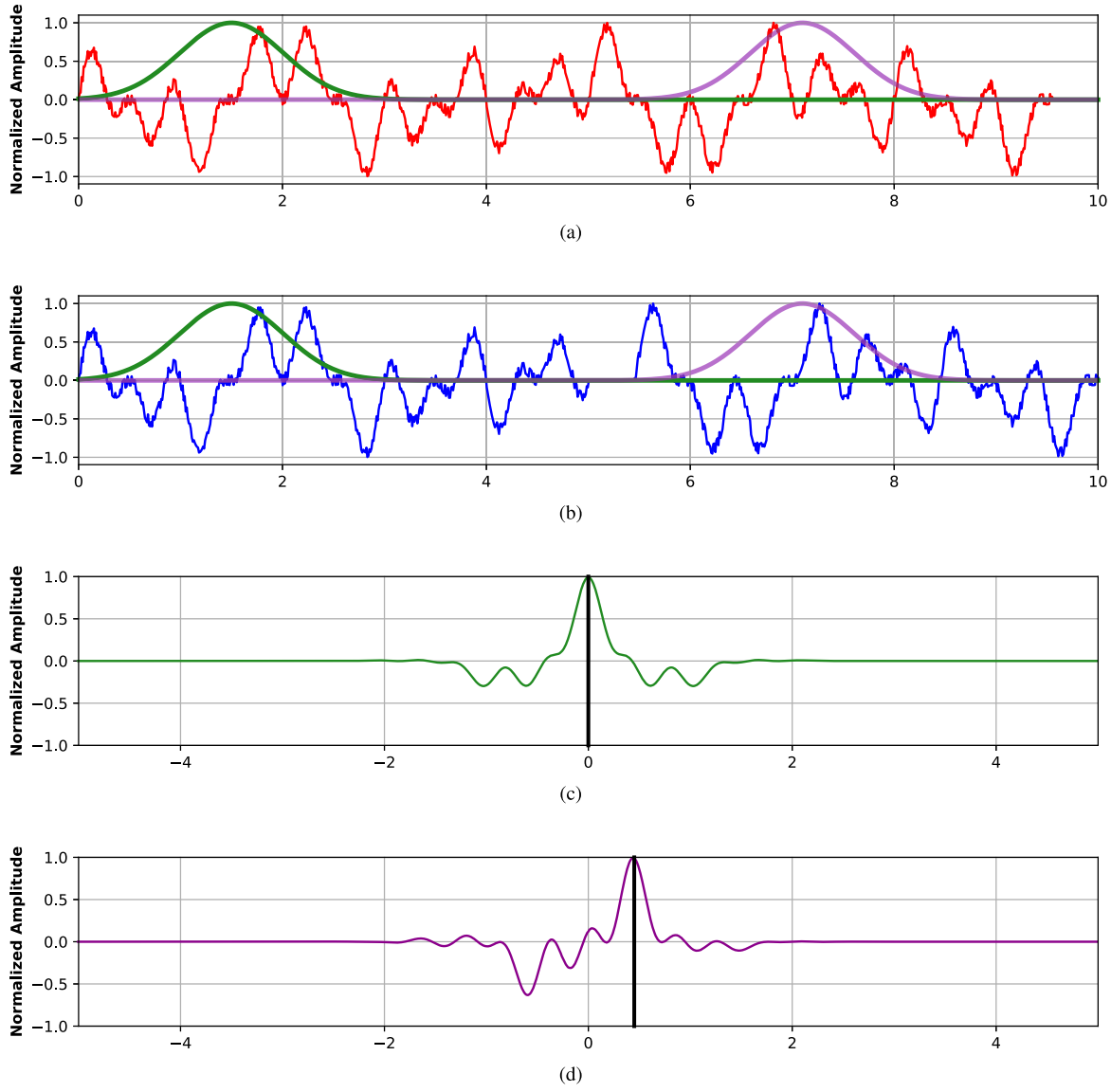


Fig. 2. (a) The synthetic signal recorded by receiver A. (b) The synthetic signal recorded by receiver B in which the second half of the signal observed by A is delayed by 0.45s. In (a) and (b), green and purple lines indicate examples of two separate Gaussian windows applied to the data. The resulting local cross-correlation from the first half of the signal created by the green window is shown in (c), and the result of the second half produced by the purple window is shown in (d). Notice that the local cross-correlation method is able to identify the travel time change in the second half of the signal while preserving the zero lag travel time in the first half.

ple the direct path, $x_A x_B$, between the two receivers in order to find the true causal and anti-causal travel times. Causal travel times are caused by waves propagating from A to B resulting in a positive time lag during cross-correlation. Anti-causal travel times correspond to waves propagating from B to A and result in an equal, but negative, time lag because of the order of the receivers in the cross-correlation. For a source at $\phi = 45°$, the source wavelet arrives at receiver A slightly before receiver B causing the cross-correlation to yield a travel time that is not representative of the separation between receivers in the receiver reference frame. In the most extreme case of sources located at $\phi = 0°$ or $\phi = 180°$, the source wavelet reaches both receivers simultaneously and the cross-correlation indicates a zero lag travel time even though the receivers are not collocated. To counteract this effect, we stack the correlation gather in Fig. 3(b) over source angle ϕ (i.e. stack each individually computed cross-correlation), to produce the correlation stack shown in Fig. 3(c) where we can observe the travel times indicated by the high-energy responses at times ± 0.5 s. By stacking over source angle, we take advantage of the strong constructive interference that occurs for sources located close to the direct path connecting the receivers, a region commonly referred to as the Fresnel zone or stationary phase zone. Wapenaar et al. (2010) provide guidelines to formally define the size of this region. The Fresnel zone is equivalent to the region of constructive interference between a wave emitted at the virtual source location and the back

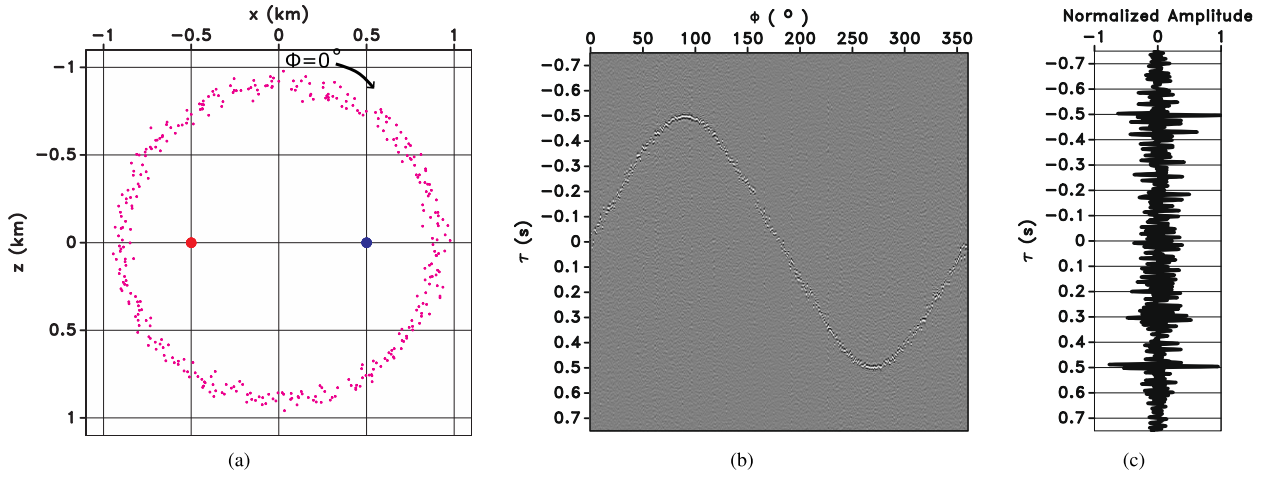


Fig. 3. (a) An isotropic source distribution surrounding two receivers shown in red and blue. The azimuthal angle of the circular source distribution is denoted by ϕ. (b) The correlation gather produced by cross-correlating the receiver responses when each source is fired independently. (c) The result produced by stacking the correlation gather over source angle ϕ. When interpreting correlation stacks, it is important to note that the definition of a cross-corrleation allows for travel times that are both positive (causal) and negative (acausal). This is because sources may be situated on either side of the receivers causing wave propagation in opposite directions. Then, the cross-correlation may indicate negative travel times that seemingly imply backward wave propagation. However, acausal components are simply a consequence of some waves arriving at B before A because of the source location.

propagation of this wave from the receiver location. Fig. 4(a) displays the Fresnel zone of the source-receiver geometry depicted in Fig. 3(a). To produce the correlation stack, we have enforced that each source be activated only after the previous wave has passed through both receivers. This ensures that only a single wave arrives at the receivers for each individual cross-correlation. However, practical applications of seismic interferometry do not allow us to determine the precise timing of sources, especially if they are produced by random processes. This becomes problematic when several sources activate simultaneously as can be seen in the correlation stack in Fig. 5(a) where we are no longer able to discern the correct travel times corresponding to the direct path between receivers A and B. In this scenario, the cross-correlation between receiver responses is complicated by the arrival of multiple events in the same listening period that produce strong correlation responses with each other. These events are commonly referred to as cross-terms and should be avoided in order to isolate the true travel time. Random persistent sources located in the Fresnel zones correspond to nearly equivalent travel times between receivers because of their phase similarity and do not contribute to this effect. For transient sources in the Fresnel zone however, cross-terms will still exist and can be mitigated by applying frequency domain filtering discussed in Section 3 or by time windowing as discussed in Appendix C.

We must enforce that only sources originating in the Fresnel zone be used in the cross-correlation. This can be accomplished through the use of an angle-of-arrival filter that preserves signals originating from specified directions. To use an angle filter, we replace the single receiver at A and B with receiver *arrays* at A and B which can be used to relate a signal's change between antenna elements to the arrival angle of the wave. Many suitable algorithms exist that rely on receiver arrays to implement angle filtering (Estimation of Signal Parameters via Rotational Invariance Techniques (ESPRIT) (Roy and Kailath, 1989), MUltiple SIgnal Classification (MUSIC) (Schmidt, 1986), Minimum Variance Distortion Response (MVDR) (Capon, 1969), $\tau - p$ transform (Radon, 1986)). Here, we utilize the $\tau - p$ transform because of its ease of implementation and robust ability to identify signals propagating in specific directions.

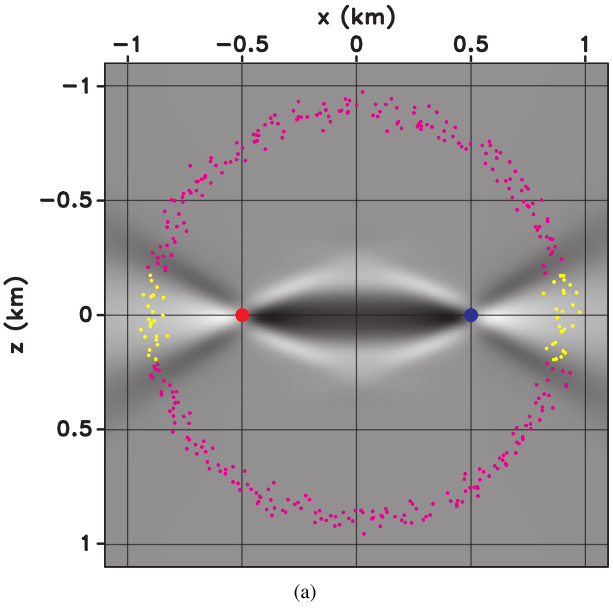
The $\tau - p$ transform converts data recorded in the time–space $(r - t)$ domain to the time-slowness $(\tau - p)$ domain where slowness, p, is defined as

$$p = \frac{\sin(\theta)}{c}. \tag{5}$$

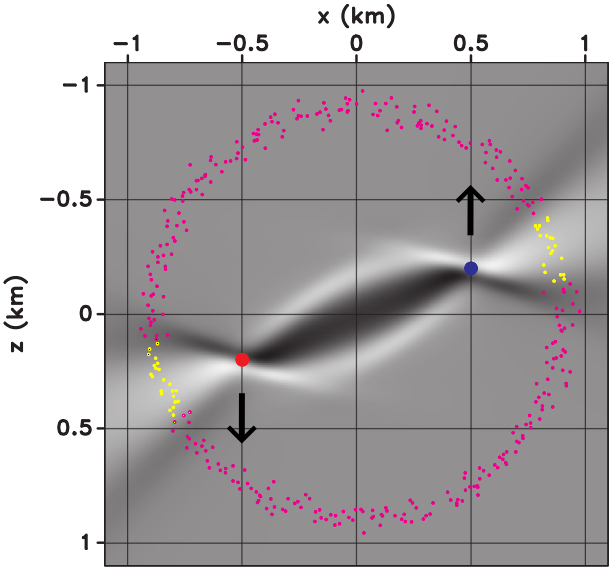
c is the medium velocity and θ is the angle-of-arrival at the receiver array defined relative to the normal to the planar antenna. We can filter for a particular angle by choosing a slowness value that corresponds to the desired angle. To incorporate contributions near the selected angle that correspond to sources located in the Fresnel zone, we apply a Gaussian window to the data in the $\tau - p$ domain centered at the desired slowness. The standard deviation of this Gaussian window is related to the size of the Fresnel zone. As a convention to determine the size of this window, we use the width of the Fresnel zone at half the distance between receivers (denoted by δ)

$$\delta = \tan^{-1}\left(\sqrt{\frac{\lambda}{L}}\right), \tag{6}$$

where λ is the wavelength of the signal and L is the distance between receivers. Appendix B includes a derivation for δ. In practice, the determination of an appropriate width for the Gaussian window is dependent on the attenuation pro-



(a)

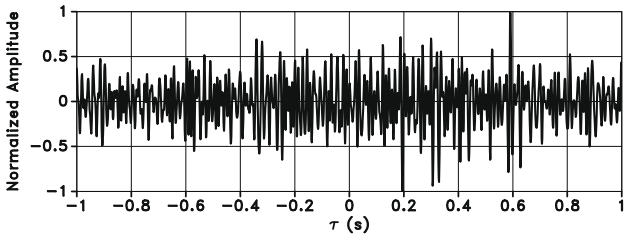


(b)

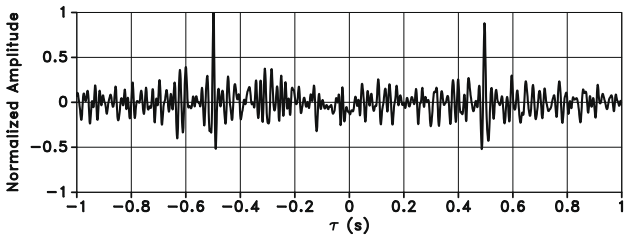
Fig. 4. (a) The Fresnel zone for a stationary receiver pair. (b) The Fresnel zone at $t = 0.3$s for a mobile receiver pair. Sources in yellow behind the receivers constructively interfere to produce high-energy responses in the correlation stack.

file of the medium which in turn controls the maximum potential offset of a source that contributes to the cross-correlation.

The data filtered in the $\tau - p$ domain can be transformed back to the $r - t$ domain with contributions from sources outside the Fresnel zone attenuated. Fig. 6(a) - (d) provide a visualization of each step in the filtering process. This process must be applied to the data collected by both receiver arrays using the appropriate angle-of-arrival. Then, we can cross-correlate the filtered data to isolate the accurate travel times between the receivers without the interference of cross-terms. Fig. 5(b) is the correlation stack created



(a)



(b)

Fig. 5. (a) The correlation stack produced when multiple sources are activated simultaneously. (b) The correlation stack shown after $\tau - p$ filtering has been applied to isolate contributions from within the Fresnel zone.

after applying an angle-of-arrival filter when multiple sources are active randomly and simultaneously.

In the case of a scattering medium, angle-of-arrival filtering between receiver arrays may struggle. This is because we implicitly assume that the angle around which to filter is defined by the angle connecting the arrays. In a weakly heterogeneous medium, the ray path between receivers is approximately straight, and thus the Gaussian window used in angle filtering can still capture the appropriate arrival. If a wave is scattered significantly in a strongly heterogeneous medium, it does not satisfy a straight ray approximation, and we cannot analytically determine the angle-of-arrival. In this case, we might instead proceed with a more computationally expensive approach in which we sweep over all angles between the two receiver arrays. A second alternative approach is to first perform reverse time migration (RTM) using data from each receiver array to build an initial rough subsurface model. This model can then be used to determine the approximate angle-of-arrival around which to filter thereby reducing our assumptions of an approximately straight path connecting receiver arrays.

In addition, when applying seismic interferometry on small planetary bodies to study the full interior structure, we cannot assume an unbounded medium as may be employed in regional-scale applications. Ruigrok et al. (2008) show that for a bounded medium, the cross-correlation of the receiver responses introduces non-physical artifacts that result from cross-terms between reflected and transmitted events. However, when performing cross-correlation between *multiple* receiver arrays, complimentary cross-terms are created by the same internal feature and have opposite phase at equivalent time lags.

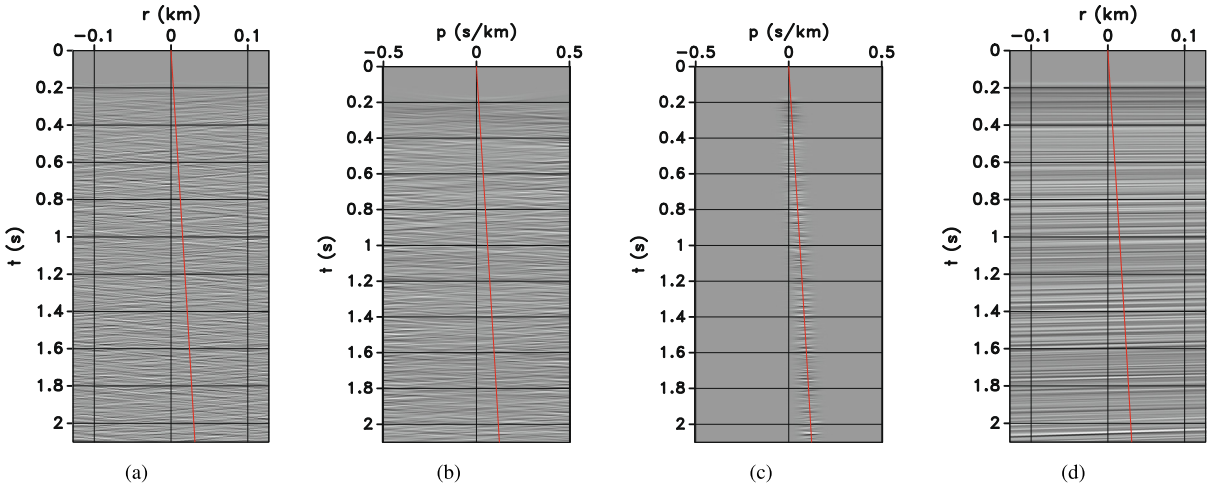


Fig. 6. (a) Data recorded by receiver array A. The horizontal axis represents the elements of the antenna array. (b) The data in panel (a) after conversion into the $\tau - p$ domain. (c) The filtered data in the $\tau - p$ domain. (d) Data transformed back to the $r - t$ domain. The red lines indicate the calculated slowness value p based on the approximate angle-of-arrival θ and medium velocity c. A Gaussian window whose standard deviation is set by the Fresnel zone angle δ is centered around p to incorporate contributions from within the Fresnel zone. Because the receivers are not stationary, the angle-of-arrival and thus the slowness change over time.

Thus, for an ideal acquisition geometry and duration, these events will destructively interfere to cancel out. Even in non-ideal acquisition, the cross-terms will not cancel completely, but the resulting artifacts may still be reduced. Conversely, in the alternative auto-correlation acquisition with a *single* receiver array mentioned in Section 3, we cannot take advantage of phase cancellation, and the non-physical cross-terms will persist.

We encounter similar challenges in lossless media as described in Draganov et al. (2010). For rays that traverse a longer path, attenuation will compound the amplitude decay more significantly than rays that traverse a shorter path. Thus, even though cross-terms from internal events will have opposing polarity, destructive phase interference will not completely cancel these events because amplitude decay is not equivalent. This is particularly relevant for reflection event retrieval since the persistence of these cross-terms can obscure the reflection amongst cross-term noise. However, the authors also show that the direct transmission response can still be recovered in a strongly attenuating medium, thereby enabling the application discussed in Section 3 where intrinsic losses may be substantial (Nishiyama et al., 2021).

2.2. Mobile interferometry

The theory presented in the preceding section relies on stationary receivers. Accounting for receiver motion requires modifications to the original seismic interferometry theory because the cross-correlation must be able to resolve a changing travel time between receivers A and B as a function of time. By incorporating receiver motion into the cross-correlation, seismic interferometry can be performed from ocean floating (i.e., MERMAIDS hydrophone arrays), airborne (i.e., Venusian atmospheric sounders), or satellite based vehicles (i.e., small body orbiting satellites) (Hello and Nolet, 2021; Krishnamoorthy and Bowman, 2023; Sava and Asphaug, 2019).

We modify the previous source receiver geometry to move the receivers at a constant velocity in opposite directions. Fig. 7(b) shows the updated receiver position at $t = 0.3$ s. As they move, the angle-of-arrival θ at the receivers, and thus the Fresnel zone, changes creating a new value of slowness p. Fig. 4(b) shows the corresponding Fresnel zone at $t = 0.3$ s. Because we have previously assumed that noise sources are isotropically distributed around our receivers, we have conveniently created sufficient coverage to ensure enough sources exist in the Fresnel zone between the receivers, even when in motion. However, we must continuously update the angle-of-arrival filter to reflect the evolving angle θ between the arrays. This can be accomplished by adapting the Gaussian mask in $\tau - p$ to vary as a function of θ. In addition to variable angles-of-arrival, the distance between receivers A and B is also variable and because the medium velocity remains fixed, the travel time between receivers changes as a function of time.

We can observe this travel time change in a 1D homogenous and lossless medium. In this example, the receiver at location x_B moves relative to the receiver at position x_A (Fig. 8(a)). The source sends a pulse at $t = 0$ which arrives at receiver A at time $t_A = \frac{x_A - x_S}{c}$ shown in Fig. 8(b). However, the impulse takes longer to arrive at B since it must catch up to the mobile receiver. The exact time of arrival as shown in Fig. 8(c) is found by

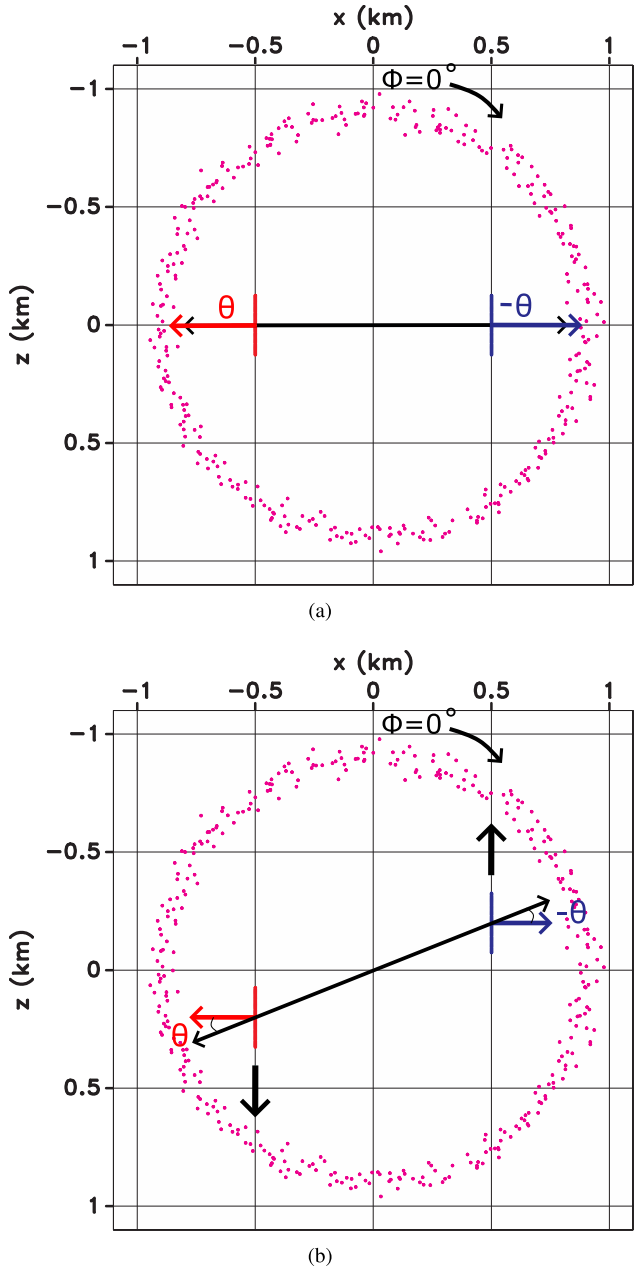


Fig. 7. (a) The initial positions of the two receiver arrays at $t = 0$s. θ represents the angle-of-arrival relative to the normal of the receiver arrays. The arrays are exactly perpendicular causing $\theta = 0$. (b) The new location of receivers after moving for a short time period. The direct path between the receivers is now at a different angle.

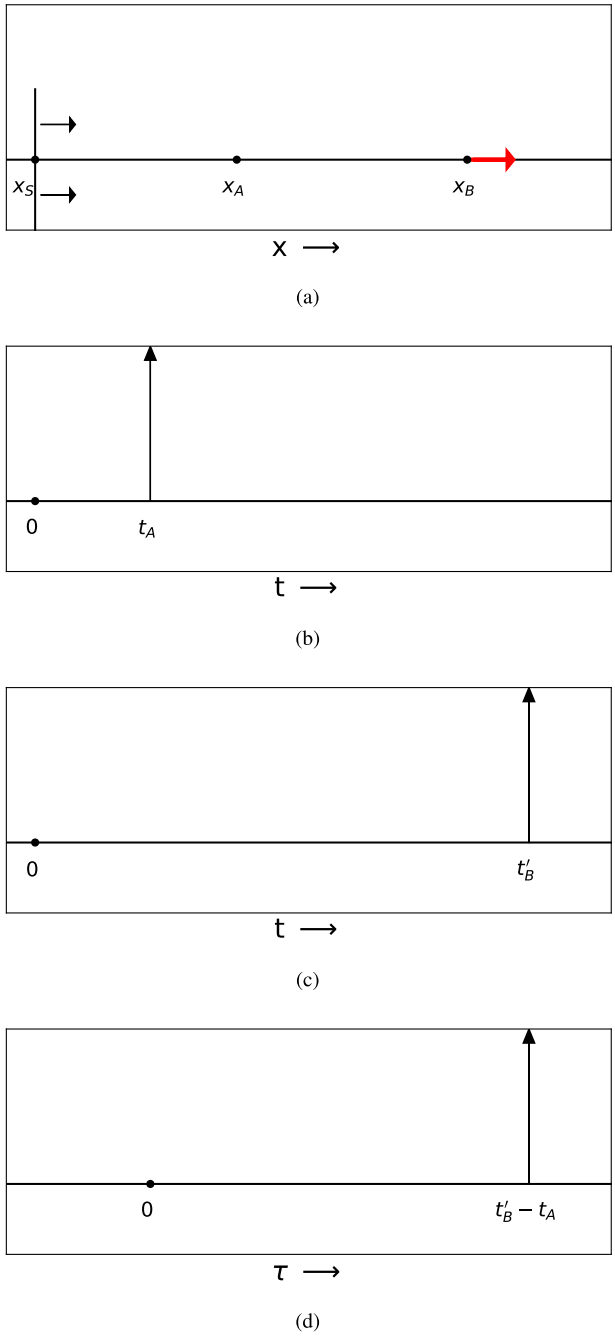


Fig. 8. A mobile 1*D* interferometry example where receiver *B* is moving away from receiver *A*. (a) A plane wave emitted at $t = 0$ and $x = x_S$. (b) The response recorded by the receiver at x_A. (c) The response recorded by the receiver at $x_B\prime$. (d) The cross-correlation of the receiver responses at positions x_A and $x_B\prime$.

$$t_B\prime = \frac{x_B\prime - x_S}{c} \tag{7}$$

$$= \frac{vt_B\prime - x_S}{c} \tag{8}$$

$$= \frac{x_S}{v - c}. \tag{9}$$

As a result of this motion, the cross-correlation in Fig. 8(d) provides the travel time between x_A and the new receiver position, $x_B\prime$. If the source were to emit another impulse as *B* continued traveling, we would observe a second travel time, $t_B\prime\prime \neq t_B\prime$, corresponding to the variable separation between x_S and $x_B\prime\prime$. Were the source to continue emitting as *B* moved further away, we would observe a new travel time for each impulse.

As receiver B moves away from A, the travel time grows increasingly larger. When applying cross-correlation using Eq. 3, we integrate the local cross-correlations to improve SNR and produce a single global cross-correlation for the entire observation period. Thus, with global cross-correlation we cannot resolve the distinct, increasing travel times. However, local cross-correlation preserves this information. Figs. 9(a) and 9(b) display the travel time between the receivers as a function of time lag τ before and after applying the stack over time t. The non-linear travel times highlighted in the unstacked data of Fig. 9(b) reflect the changing separation between the receivers. Red dashed lines represent the analytically derived travel time between the receivers as a function of time. The coincidence of the analytical and numerical solutions demonstrates the accuracy of the local cross-correlation method.

Whereas a stacked cross-correlation obfuscates the correct travel times, the unstacked local cross-correlation method identifies the variable travel times produced by moving receivers. However, to accomplish this, we sacrifice SNR improvements achieved in the global cross-correlation by summation over time. This is a critical step in the development of seismic interferometry for mobile receivers and enables the new exploration geometry dis-

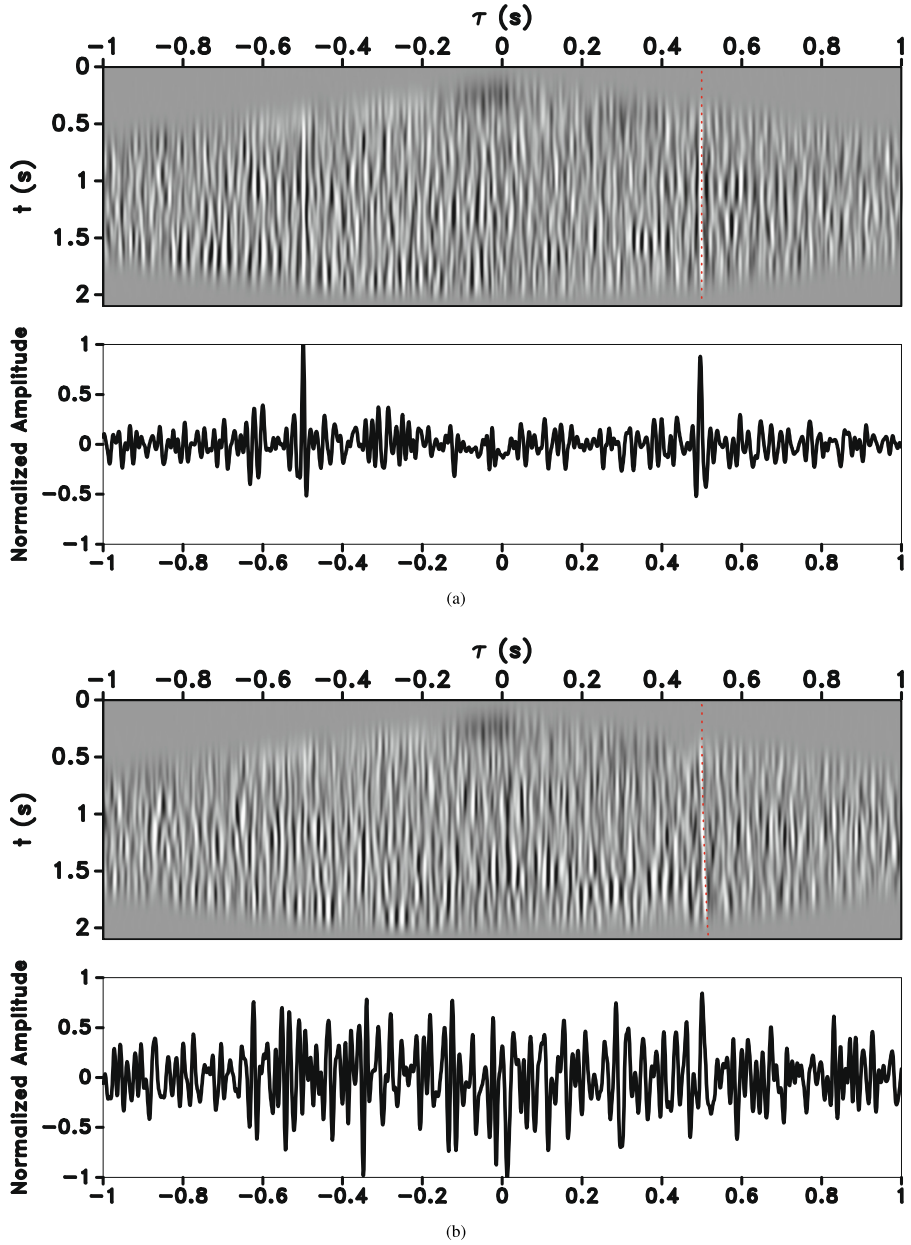


Fig. 9. The stacked and unstacked local cross-correlation plots for stationary (a) and mobile (b) receivers. Red lines indicate the analytically derived travel times for this model. The result of the unstacked cross-correlation operation is shown in the top plots of (a) and (b), while the bottom panels provide the same data stacked over observation duration. For stationary receivers, the travel time between the receivers remains constant, so stacking simply improves SNR. The red dashed lines indicate the analytically derived travel times for each time step in this model.

cussed below. Although the underlying seismic interferometry technique remains the same, the modified version presented here has several key additions. In traditional seismic interferometry, we first record ambient noise by one or more stationary receivers and then compute a global cross-correlation to calculate the constant travel time between receivers. Modified seismic interferometry theory requires several extra sequential steps: (a) record ambient noise with one or more receiver *arrays*; (b) apply angle-of-arrival filtering; (c) perform local cross-correlation of the filtered data; (d) perform coherence filtering; (e) observe time-varying receiver travel times. By including these steps, we can now estimate the changing travel time between receivers as a function of time.

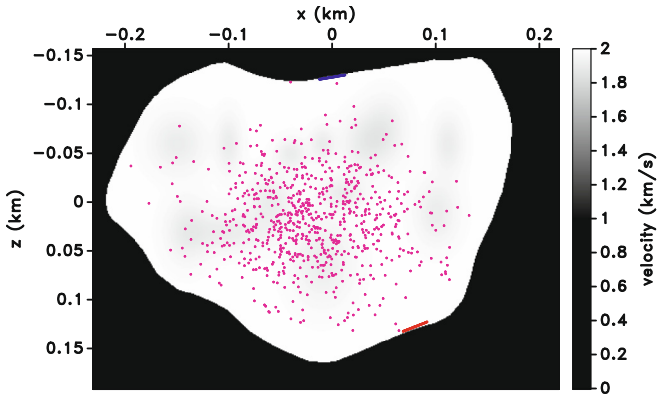


Fig. 10. A 2D shape model of asteroid 99942 Apophis (Brozovic et al., 2018). Purple dots are the locations of random sources. Density contrasts, displayed in light gray, are also randomly distributed throughout the model interior to mimic boulder aggregations in the subsurface structure. Red and blue lines denote the initial positions of the two receiver arrays.

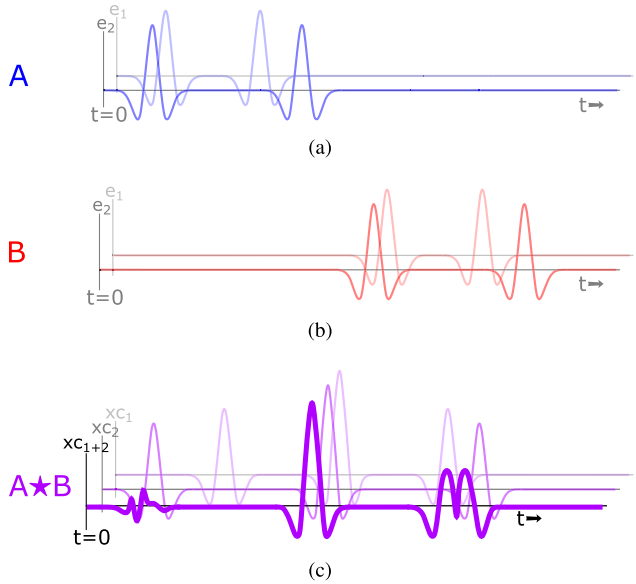


Fig. 11. (a) The responses recorded by receiver A from two separate double pulse source experiments, e_1 and e_2. (b) The data recorded by receiver B from the same sources. (c) xc_1 and xc_2 are the cross-correlations when the double pulse experiments are cross-correlated *independently*, i.e., $xc_1 = e_{1,A} \star e_{1,B}$ and $xc_2 = e_{2,A} \star e_{2,B}$. The bold trace, xc_{1+2}, is the cross-correlation of what receivers A and B record, a superposition of the two double pulse experiments $xc_{1+2} = e_{1+2,A} \star e_{1+2,B}$.

3. Application to a small planetary body

We apply the local cross-correlation method developed in Hale (2006) to estimate the direct travel time between receiver arrays and demonstrate the ability to recover time-varying travel times. We use the Madagascar finite-difference modeling package to create wavefield simulations (Fomel et al., 2013), and, using mobile LDVs capable of recording ambient seismicity from orbit, consider data acquisition on a small planetary body like asteroid 99942 Apophis. We note that a complimentary approach using just one LDV instrument can acquire data at a unique surface location to compute auto-correlations. This enables the retrieval of body-wave reflections as demonstrated by Nishitsuji et al. (2016) using conventional seismometers on the Moon. However, to reobserve the same surface location requires precise ground-track repeats that may be difficult to achieve around a complex target. For this reason, we exclusively discuss the deployment of two array LDVs that observe seismic activity initiated by natural events.

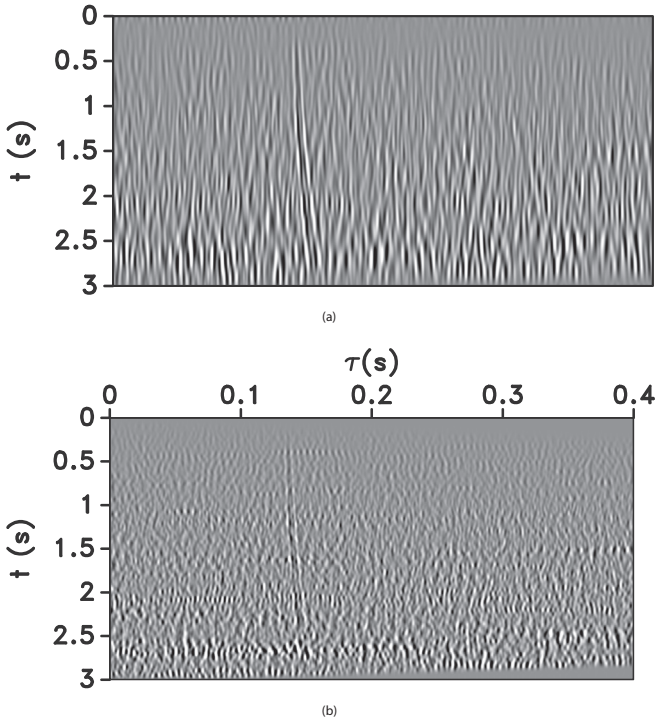


Fig. 12. (a) The unstacked local cross-correlation after frequency filtering has been applied. (b) The unstacked local cross-correlation prior to applying frequency filtering. The receiver array in Fig. 10 is not situated directly at the surface of the asteroid because of model grid constraints. As a result, there is a second strong travel time shortly after the primary. This artifact is caused by a reflection off the surface of the asteroid that passes back through the receiver array and would not be present in a true acquisition scenario because the receivers would observe the surface.

Local cross-correlation of the LDV data provides the direct travel time response between points on the surface.

Fig. 10 shows a 2D shape model of 99942 Apophis used in subsequent wavefield simulations where we assume an interior structure with variable velocity. Model boundaries are defined by extracting a cross-section from the 3D radar shape model produced by Brozovic et al. (2018). A 2D representation is used to reduce computational complexity, but expansion into 3D is straightforward from the original model. This simulation uses 721 sources with frequencies centered between 60 Hz and 90 Hz that are randomly distributed throughout the model interior to mimic the presence of naturally occurring seismic sources. Appendix D provides further details on this choice of source characteristics. These sources fire at random times throughout the model while two receiver arrays record the subsequent seismic activity at the surface of the asteroid. Because attenuation of small bodies are not constrained by in situ measurements (Asphaug, 2008), we apply an exponential attenuation decay as a function of model time. This ensures that the seismic activity does not continuously grow in amplitude causing the model to become unstable.

We perform angle-of-arrival filtering (Eq. 5) on each receiver array to isolate the contributions of sources located in the Fresnel zone between the receivers. Because our receivers are in motion, we vary the angle-of-arrival filter to reflect the time varying Fresnel zone discussed in Section 2. After computing the local cross-correlation, spurious noise is still present in the data. This noise originates from sources within the Fresnel zone that continu-

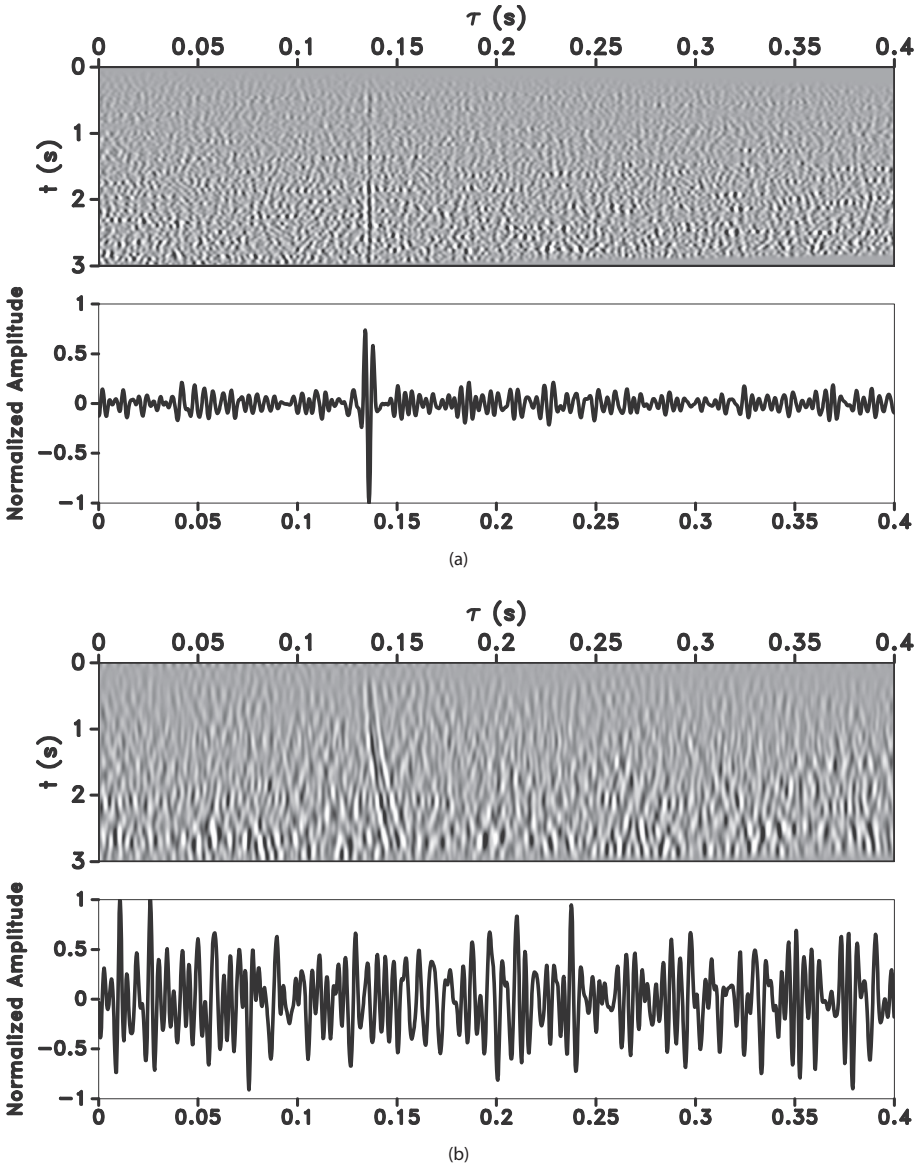


Fig. 13. The unstacked and stacked local cross-correlation for simulated stationary (a) and mobile (b) LDVs orbiting asteroid 99942 Apophis. The top plots are the unstacked local cross-correlation, while the bottom plots are the same data stacked over the duration of observation. Notice that the correlation stack does not allow us to observe the variable travel time as the receivers orbit the target.

ously fire thus creating more cross-terms. Fig. 11(a) - (c) illustrates this phenomenon with a source that is fired twice in quick succession (double pulse source). Because sources are random, the time between the double pulses varies. After cross-correlation, the coherence of the wavelet corresponding to the accurate travel time remains strong because the travel time is the same for any source in the Fresnel zone. However, the coherence of the cross-terms degrades because their cross-correlation produces different travel times that superpose together. When viewing the local cross-correlation, these cross-terms appear as high frequency jittering in the data. To remove this noise, we Fourier transform both the time t and time lag τ axes and implement a frequency-frequency domain angle filter that preserves constant frequencies. Figs. 12(a) and 12(b) show the causal part of the local cross-correlation before and after frequency filtering. The result of seismic interferometry, after applying this additional processing step, is shown in Figs. 13(a) and 13(b) for both stationary and mobile receivers, respectively. The local cross-correlation enables us to observe the evolving travel time between receivers that is caused by the spacecrafts' motion around the asteroid. The correlation stack does not preserve the variable travel time as the receivers orbit the target but instead smears them together into a noisy signal. To accurately estimate the travel time between the receivers, we must use receiver arrays in addition to unstacked local cross-correlations. Receiver arrays enable angle-of-arrival filtering necessary to remove the contributions of sources outside the Fresnel zone, while unstacked local cross-correlations allow us to observe the varying travel time between receivers. Without these two components, the cross-correlation is not capable of isolating the correct travel time and subsequent models produced by travel time tomography will not be representative of the true subsurface structure.

4. Conclusions

We have modified the seismic interferometry method to use an acquisition system with mobile receivers and demonstrated the procedure in a representative, simplified 2D asteroid encounter. To accommodate mobile acquisition, we revise the basic tenets of seismic interferometry with stationary receivers to account for realistic random source behavior. In ambient seismic interferometry, random sources fire simultaneously and from many directions. Waves arriving at the receiver arrays at the same time but from different directions disrupt the recovery of the accurate travel time by introducing cross-terms. To mitigate this, we replace single receivers with receiver arrays that allow us to perform angle-of-arrival filtering on incoming signals to isolate the contributions of random sources located in the Fresnel zone. To account for the motion of the receivers, we vary the angle filter with time to reflect the changing relative positions of the arrays.

However, the global cross-correlation of directionally filtered data alone is still insufficient to resolve the correct travel time between mobile receivers. As receivers move, the distance between them changes resulting in time-varying travel times. Global correlation stack smears these different travel times together resulting in a noisy signal that does not accurately represent the true time-variable propagation paths. For this reason, we use an unstacked local cross-correlation to accurately obtain the varying travel time between receivers. We also introduce frequency-frequency domain angle filtering to repress the interference of repetitive sources located in the Fresnel zone that cause additional cross-terms that persist even after angle-of-arrival filtering.

By combining these acquisition geometry and processing modifications, we use a numerical model to show successful travel time recovery using ambient seismic interferometry with mobile receivers. These results demonstrate a potentially powerful new tool for acquiring seismic data from mobile platforms. Future work is needed to advance this foundation into 3D for the proposed orbit around a small, naturally active planetary body. In addition to the application demonstrated here for asteroids, these results advance a potentially powerful new tool for seismic data acquisition with ocean-floating seismometers and airborne or balloon-borne seismometers on Earth, Titan or Venus (Krishnamoorthy and Bowman, 2023).

Declaration of Competing Interest

The authors declare that they have no known competing financial interests or personal relationships that could have appeared to influence the work reported in this paper.

Acknowledgments

This research is supported by the sponsors of the Center for Wave Phenomena at Colorado School of Mines. We are grateful to Roel Snieder for his support in developing the theory of mobile seismic interferometry and Andryw Wade for acquiring the displacement data used in Appendix D. We also thank Matthew Siegfried for his editorial contributions. The reproducible numeric examples used the Madagascar open-source software package (Fomel et al., 2013), freely available from www.ahay.org.

Appendix A. Local cross-correlation

This appendix summarizes local cross-correlation. To derive the centered local cross-correlation form, we begin with the uncentered local cross-correlation expression that relies on Gaussian windows to reduce the observed data into small segments. The windows are centered at the same sample location in each receiver recording and the cross-correlation is computed to produce a single value. Then, we slide the windows forward in time to the next sample location and repeat this process. Gaussian windows are

particularly advantageous because they retain high resolution in the windowed data and because the product of two Gaussian windows yields one single Gaussian window allowing us to simplify the cross-correlation expression. Moreover, Gaussian windows are easily extensible to multiple dimensions and benefit from fast recursive filter implementation (Hale, 2006).

The general uncentered definition of the local cross-correlation is

$$c(\gamma;\tau) = \int_0^t u_A(t)g(\gamma - t)u_B(t+\tau)g(\gamma - t + \tau)dt, \tag{A.1}$$

where $u_A(t)$ and $u_B(t)$ are the signals recorded at receivers A and B respectively, and $g(t)$ are the Gaussian windows acting on each of the signals. We can simplify this expression by taking advantage of the product of two Gaussians yielding a single Gaussian:

$$c(\tau) = \int_0^\gamma \int_0^t u_A(t)u_B(t+\tau)g(\gamma - t;\tau)dtd\gamma. \tag{A.2}$$

It is common to use a centered cross-correlation that is created by shifting one signal forward by $\tau/2$ and the other signal back by $\tau/2$. This method is equivalent to the uncentered cross-correlation where only one signal is shifted forward by τ. Modifying Eq. A.2 to form a centered local cross-correlation, we obtain

$$c(\tau) = \int_0^\gamma \int_0^t u_A(t-\tau/2)u_B(t+\tau/2)g(\gamma - t;\tau)dtd\gamma, \tag{A.3}$$

where $u_A(t-\tau/2)$ and $u_B(t+\tau/2)$ are the half-step shifted signals. If we integrate this expression over γ, we produce the centered local cross-correlation

$$c(\gamma;\tau) = \int_0^t u_A(t-\tau/2)u_B(t+\tau/2)g(\gamma - t;\tau)dt, \tag{A.4}$$

that allows us to observe time varying travel times between receivers.

Appendix B. The Fresnel zone

Estimating the angle of deflection of the diffracted wave that produces constructive interference between two receivers is critical for angle-of-arrival filtering because it determines the standard deviation of the Gaussian window used in angle domain filtering. Spetzler and Snieder (2004) provide a derivation for the regions of constructive interference between two receivers. They show that the path length difference (D) between the direct wave and the diffracted wave is given by

$$D \approx \frac{1}{2}\left(\frac{1}{x} + \frac{1}{L-x}\right)q^2(x), \tag{B.1}$$

where $q(x)$ is the vertical deflection of the diffracted wave measured relative to the direct wave connecting the receivers, L is the distance between the receivers, and x is the distance of the diffracting point from the virtual source (Fig. B.14). Primary constructive contributions arise when a diffracted wave and direct ray have a path length difference that is small compared to the wavelength λ

$$D < \lambda/n, \tag{B.2}$$

where n is the fraction of the wavelength that can still provide constructive interference of waves. If we choose $n = 2$ indicating constructive interference from a half wavelength and solve for the diffracting point that is half the distance between the receivers, we find the condition for constructive interference is

$$q(x) = \sqrt{\frac{\lambda x(L-x)}{L}} \tag{B.3}$$

$$= \sqrt{\frac{\lambda \frac{L}{2}(L-\frac{L}{2})}{L}} \tag{B.4}$$

$$= \frac{\sqrt{\lambda L}}{2}. \tag{B.5}$$

We can then calculate the angle of deflection of the diffracted wave that produces constructive interference by

$$\tan(\delta) = \frac{q(x)}{x} \tag{B.6}$$

$$= \frac{\sqrt{\lambda L}/2}{L/2} \tag{B.7}$$

$$= \sqrt{\frac{\lambda}{L}}, \tag{B.8}$$

where δ is used to determine the angular width of the Fresnel zone between the receivers. We also use this angle to derive the standard deviation of the Gaussian window during angle-of-arrival filtering in the $\tau - p$ domain which allows us to incorporate constructive contributions from sources within the Fresnel zone.

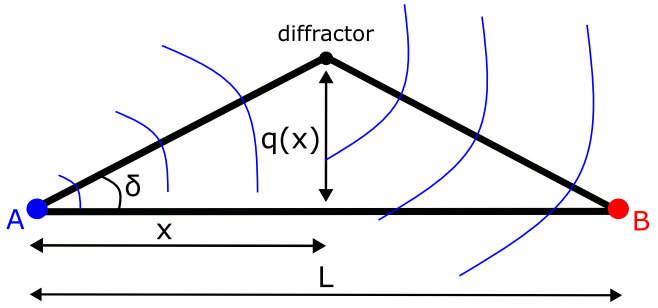


Fig. B.14. The angle of deflection geometry of the diffracted wave (shown in blue). The wave is emitted from A and, after diffraction, travels to B. The diffracting point is a horizontal distance x from the virtual source and is displaced from the direct path connecting the receivers by $q(x)$. The distance between the receivers is L.

Appendix C. Source characteristics in the Fresnel zone

For *transient* noise isolated in the Fresnel zone, cross-terms can still be created. Fig. C.15 provides an example of such non-physical cross-terms resulting from the interaction of two sources. In this figure, ΔT represent the time interval between the arrival from each of the sources and

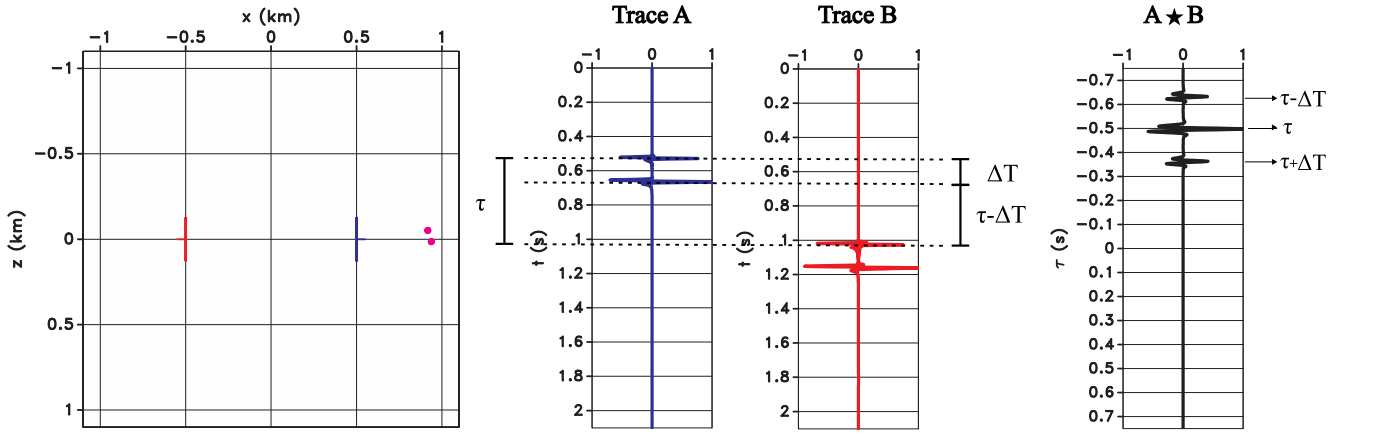


Fig. C.15 (Left) Acquisition geometry with two simultaneous, pulsed sources located in the Fresnel zone. (Middle) The data recorded by receivers A and B. T is the time difference between the two source pulses and τ is the time lag between the two receivers. (Right) The cross-correlation of the data from A and B.

τ is the time lag between the two receivers. In seismic interferometry, we are only interested in recovering τ. To accomplish this, we may employ a window and stack technique that decomposes the data into small segments, computes cross-correlations, and then stacks all correlations together to highlight the time lag (Girard and Shragge, 2020). With a time window less than ΔT, the contribution of each individual source is preserved without creating non-physical events. In the case of a *persistent* source, Δt between pulses tends to zero. As a result, the non-physical cross-term at $\tau - \Delta t$ and $\tau + \Delta t$ converge to τ and the cross-correlation of persistent sources becomes indistinguishable from the cross-correlation of a single source.

Appendix D. Laser Doppler vibrometer sensitivity

The observable Doppler shift depends on ground velocity (describing particle motion) which is intrinsically related to the wave frequency and amplitude. Plausible seismic velocities in a small body range from 1×10^2 ms^{-1} to 1×10^3 ms^{-1} based on the characteristics of Lunar regolith in lieu of data from a small planetary body (Watkins and Kovach, 1973). Thus we choose *relevant* seismic wavelengths relative to the body diameter, e.g., from 1% to 50 %, to guarantee high resolution imaging at one end, and for the waves to be bounded by the body itself at the other end. Apophis' smallest axis is roughly 170 m in diameter. Accordingly, the high-end of frequencies that we record is 176 Hz for regolith velocity of 300 ms^{-1} and wavelengths that are 1 % of the axis diameter. Conversely, the lowest frequency we might use for seismic imaging is 0.8 Hz occurring on the longest axis (450 m) with seismic velocity of 200 ms^{-1} and a wavelength that is 50 % of the axis diameter. We choose simulation frequencies (centered at 75 Hz) that fall in this range to match the acquisition requirements described here.

In addition to estimating the seismic bandwidth we aim to record, we can also characterize ground displacement usable for seismic experiments. Displacement due to a seismic wave has an upper bound at which a surface material (like a boulder) loses attachment to the ground. When this occurs, the experiment no longer characterizes seismic energy propagating inside the body, but rather provides information on the cohesion of the surface regolith. In microgravity, ground attachment is modulated by cohesion forces which are potentially greater than gravity forces (Scheeres et al., 2010). Cohesion of an embedded boulder depends on its size d, density ρ, and cohesion c which we estimate in the range of 1 Pa to 1×10^3 Pa consistent with the Hayabusa2 estimates from SCI at the low end (Arakawa et al., 2020). The maximum seismic displacement at which a boulder loses attachment to the surface is

$$\bar{u} = \frac{3c}{\rho d} \frac{1}{(2\pi f)^2}. \tag{D.1}$$

For surfaces primarily composed of regolith with weak particle cohesion, energy transfer to the regolith may be weak and the subsequent displacement small. An LDV with appropriately high frequency (and thereby displacement sensitivity) must be selected as a mission design

parameter to capture anticipated displacements. This engineering requirement necessitates further research on the anticipated surface properties of small bodies. An alternative mission design could observe a single, large ground feature (e.g., boulder) over a partial orbital period as proposed in Sava and Asphaug (2019). This concept sacrifices spatial coverage and subsurface illumination for improved displacement measurements. Such a tradeoff could be determined on-the-fly by the mission team depending on LDV hardware specifications and initial observations of the regolith.

Furthermore, we constrain the operating range of a laser Doppler vibrometer assumed to be operating in an atmosphereless environment. Placing a lens of focal length f at distance L from the target surface, the light flux at a short-range D matches the light flux at a long range $R = \frac{D+L(D-L)}{f}$. We simulate acquisition at ~ 1 km by placing a telescope at $D = 10$ m. Fig. D.16 plots test data obtained from a 100 mW source powered laser recording at various distances. The reflecting target was a mechanical vibrating generator set at 2 Hz with 10 μm amplitude. The recovered seismograms are identical, even though the reflected power to the detector varies by orders of magnitude.

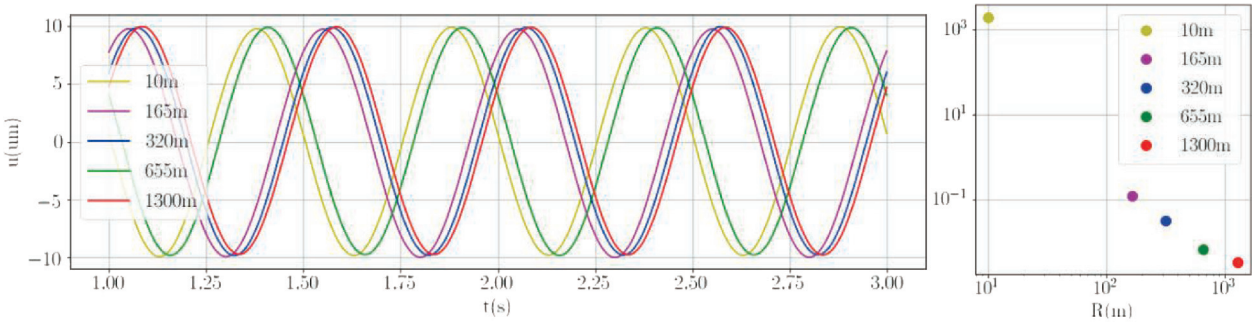


Fig. D.16 Displacement data obtained from a 100mW source laser recording at various distances. The displacement time series (left) are color-coded with corresponding received power (right).

Asteroid surfaces are usually dark (Nesvorný et al., 2015), with albedo ranging from 3 % to 30 % depending on the material type and the intensity of the reflected laser beam is scaled proportionally to surface albedo. Nevertheless, an appropriately constructed LDV with wide telescope aperture (tens of cm) and sensitive light sensors can operate well at distances of kilometers for surfaces with albedos in the single percent range.

References

Acciari, V.A., Bernardos, M.I., Colombo, E., et al., 2019. Optical intensity interferometry observations using the MAGIC Imaging Atmospheric Cherenkov Telescopes. Mon. Not. R. Astron. Soc. 491 (2), 1540–1547. https://doi.org/10.1093/mnras/stz3171.

Arakawa, M., Saiki, T., Wada, K., et al., 2020. An artificial impact on the asteroid (162173) Ryugu formed a crater in the gravity-dominated regime. Science 368 (6486), 67–71. https://doi.org/10.1126/science.aaz1701.

Asphaug, E., 2004. Interior structures for asteroids and cometary nuclei. In: Belton, M.J.S., Morgan, T.H., Samarasinha, N.H., Yeomans, D.K. (Eds.), Mitigation of Hazardous Comets and Asteroids. Cambridge University Press, pp. 66–103. https://doi.org/10.1017/CBO9780511525049.

Asphaug, E., 2008. Critical crater diameter and asteroid impact seismology. Meteor. Planet. Sci. 43 (6), 1075–1084. https://doi.org/10.1111/j.1945-5100.2008.tb00694.x.

Asphaug, E., 2009. Growth and evolution of asteroids. Annu. Rev. Earth Planet. Sci. 37, 413–448. https://doi.org/10.1146/annurev.earth.36.031207.124214.

Asphaug, E., Ryan, E.V., Zuber, M.T., 2002. Asteroid interiors. In: W.F. Bottke, A. Cellino, P. Paolicchi, & R.P. Binzel (Eds.), Asteroids III (pp. 463–484). University of Arizona Press. https://www.jstor.org/stable/j.ctv1v7zdn4.

Barnouin, O., Daly, M., Palmer, E., et al., 2019. Shape of (101955) Bennu indicative of a rubble pile with internal stiffness. Nat. Geosci. 12, 1. https://doi.org/10.1038/s41561-019-0330-x.

Binzel, R.P., A'Hearn, M., Asphaug, E. et al., 2003. Interiors of small bodies: foundations and perspectives. Planet. Space Sci., 51(7), 443–454.https://www.sciencedirect.com/science/article/pii/S0032063303000515.

Brownlee, D.E., Joswiak, D.J., 2017. Diversity of the initial rocky planetary building materials at the edge of the solar system. Meteor. Planet. Sci. 52 (3), 471–478. https://doi.org/10.1111/maps.12804.

Brozovic, M., Benner, L.A., McMichael, J.G., et al., 2018. Goldstone and Arecibo radar observations of (99942) Apophis in 2012–2013. Icarus 300, 115–128. https://doi.org/10.1016/j.icarus.2017.08.032.

Capon, J., 1969. High-resolution frequency-wavenumber spectrum analysis. Proc. IEEE 57 (8), 1408–1418. https://doi.org/10.1109/PROC.1969.7278.

Claerbout, J.F., 1968. Synthesis of a layered medium from its acoustic transmission response. Geophysics 33 (2), 264–269. https://doi.org/10.1190/1.1439927.

Clinton, J.F., Heaton, T.H., 2002. Potential advantages of a strong-motion velocity meter over a strong-motion accelerometer. Seismol. Res. Lett. 73 (3), 332–342. https://doi.org/10.1785/gssrl.73.3.332.

Day, J.M., 2016. Planet formation processes revealed by meteorites. Geol. Today 31 (1), 12–20. https://doi.org/10.1111/gto.12082.

DellaGiustina, D., Emery, J., Golish, D., et al., 2019. Properties of rubble-pile asteroid (101955) bennu from osiris-rex imaging and thermal

analysis. Nat. Astron. 3 (4), 341–351. https://doi.org/10.1038/s41550-019-0731-1.

DellaGiustina, D.N., Ballouz, R., Walsh, K.J., et al., 2024. Seismology of rubble-pile asteroids in binary systems. Mon. Not. R. Astron. Soc. 528 (4), 6568–6580. https://doi.org/10.1093/mnras/stae325.

Draganov, D., Ghose, R., Ruigrok, E. et al., 2010. Seismic interferometry, intrinsic losses and q-estimation. Geophys. Prospect., 58(3), 361–373. https://onlinelibrary.wiley.com/doi/abs/10.1111/j.1365-2478.2009.00828.x.

Fomel, S., Sava, P., Vlad, I., et al., 2013. Madagascar: open-source software project for multidimensional data analysis and reproducible computational experiments. J. Open Res. Software 1 (1), e8. https://doi.org/10.5334/jors.ag.

Fu, Y., Guo, M., Phua, P.B., 2011. Multipoint laser Doppler vibrometry with single detector: principles, implementations, and signal analyses. Appl. Opt. 50 (10), 1280–1288. https://doi.org/10.1364/AO.50.001280, URL: https://opg.optica.org/ao/abstract.cfm?URI=ao-50-10-1280.

Girard, A.J., Shragge, J., 2020. Automated processing strategies for ambient seismic data. Geophys. Prospect., 68(1), 293–312.https://onlinelibrary.wiley.com/doi/abs/10.1111/1365-2478.12794.

Girard, A.J., Shragge, J., Olofsson, B., 2023. Low-frequency ambient ocean-bottom node surface-wave seismology: A Gulf of Mexico case history. Geophysics 88 (1). https://doi.org/10.1190/geo2021-0732.1.

Graves, K.J., Minton, D.A., Hirabayashi, M. et al. (2018). Resurfacing asteroids from yorp spin-up and failure. Icarus, 304, 162–171.https://www.sciencedirect.com/science/article/pii/S0019103517301380. doi:10.1016/j.icarus.2017.08.025. Asteroids and Space Debris.

Graves, K.J., Minton, D.A., Molaro, J.L., et al., 2019. Resurfacing asteroids from thermally induced surface degradation. Icarus 322, 1–12. https://doi.org/10.1016/j.icarus.2019.01.003.

Greenwood, R.C., Burbine, T.H., Franchi, I.A., 2020. Linking asteroids and meteorites to the primordial planetesimal population. Geochim. et Cosmochim. Acta, 277, 377–406.https://www.sciencedirect.com/science/article/pii/S0016703720301058. doi:10.1016/j.gca.2020.02.004.

Hale, D., 2006. An efficient method for computing local cross-correlations of multi-dimensional signals. Technical Report Center for Wave Phenomena, Colorado School of Mines.

Hello, Y., Nolet, G., 2021. Floating seismographs (MERMAIDS). In: Gupta, H.K. (Ed.), Encyclopedia of Solid Earth Geophysics. Springer International Publishing, pp. 395–399. https://doi.org/10.1007/978-3-030-58631-7_248.

Herique, A., Agnus, B., Asphaug, E. et al., 2018a. Direct observations of asteroid interior and regolith structure: Science measurement requirements. Adv. Space Res., 62(8), 2141–2162.https://www.sciencedirect.com/science/article/pii/S0273117717307585. doi:10.1016/j.asr.2017.10.020.

Herique, A., Agnus, B., Asphaug, E. et al. (2018b). Direct observations of asteroid interior and regolith structure: Science measurement requirements. Advances in Space Research, 62(8), 2141–2162. URL: doi:10.1016/j.asr.2017.10.020. doi:10.1016/j.asr.2017.10.020.

Hole, J.A., 1992. Nonlinear high-resolution three-dimensional seismic travel time tomography. J. Geophys. Res.: Solid Earth 97 (B5), 6553–6562. https://doi.org/10.1029/92JB00235.

Krishnamoorthy, S., Bowman, D.C., 2023. A "floatilla" of airborne seismometers for Venus. Geophys. Res. Lett. 50 (2). https://doi.org/10.1029/2022GL100978, e2022GL100978.

Marchis, F., Kaasalainen, M., Hom, E., et al., 2006. Shape, size and multiplicity of main-belt asteroids: I. keck adaptive optics survey. Icarus 185 (1), 39–63. https://doi.org/10.1016/j.icarus.2006.06.001.

Marzari, F., Davis, D., & Vanzani, V. (1995). Collisional evolution of asteroid families. Icarus, 113(1), 168–187. URL: https://www.sciencedirect.com/science/article/pii/S0019103585710147. doi:10.1006/icar.1995.1014.

Mehta, K., Snieder, R., Calvert, R., et al., 2008. Acquisition geometry requirements for generating virtual-source data. In Seismic Interferometry: History and Present Status. Society of Exploration Geophysicists. https://doi.org/10.1190/1.9781560801924.

Michel, P., Benz, W., Richardson, D., 2003. Disruption of fragmented parent bodies as the origin of asteroid families. Nature 421, 608–611. https://doi.org/10.1038/nature01364.

Michel, P., DeMeo, F.E., & Bottke, W.F. (Eds.) (2015). Asteroids IV. University of Arizona Press. URL: http://www.jstor.org/stable/j.ctt18gzdvc.

Minton, D.A., Malhotra, R., 2010. Dynamical erosion of the asteroid belt and implications for large impacts in the inner solar system. Icarus 207 (2), 744–757. https://doi.org/10.1016/j.icarus.2009.12.008.

Molaro, J.L., Hergenrother, C.W., Chesley, S.R. et al. (2020a). Thermal fatigue as a driving mechanism for activity on asteroid Bennu. Journal of Geophysical Research: Planets, 125(8). URL: doi: 10.1029/2019JE006325. doi:10.1029/2019JE006325.

Molaro, J.L., Walsh, K.J., Jawin, E.R. et al. (2020b). In situ evidence of thermally induced rock breakdown widespread on Bennu's surface. Nature Communications, 11(2913). URL: doi: 10.1038/s41467-020-16528-7. doi:10.1038/s41467-020-16528-7.

Murdoch, N., Hempel, S., Laurent, S.P., et al., 2017. Probing the internal structure of the asteriod Didymoon with a passive seismic investigation. Planet. Space Sci. 144, 89–105. https://doi.org/10.1016/j.pss.2017.05.005.

Nesvorný, D., Broz, M., Carruba, V., 2015. Identification and dynamical properties of asteroid families. In Asteroids IV. University of Arizona Press. https://doi.org/10.2458/azu_uapress_9780816532131-ch016, URL: https://doi.org/10.2458/azu_uapress_9780816532131-ch016.

Nishitsuji, Y., Rowe, C.A., Wapenaar, K. et al. (2016). Reflection imaging of the moon's interior using deep-moonquake seismic interferometry. Journal of Geophysical Research: Planets, 121(4), 695–713. URL: https://agupubs.onlinelibrary.wiley.com/doi/abs/10.1002/2015JE004975. doi: 10.1002/2015JE004975.

Nishiyama, G., Kawamura, T., Namiki, N. et al. (2021). Simulation of seismic wave propagation on asteroid ryugu induced by the impact experiment of the hayabusa2 mission: Limited mass transport by low yield strength of porous regolith. Journal of Geophysical Research: Planets, 126(2), e2020JE006594. URL: https://agupubs.onlinelibrary.wiley.com/doi/abs/10.1029/2020JE006594. doi: 10.1029/2020JE006594. E2020JE006594 2020JE006594.

Pettinelli, E., Cosciotti, B., Lauro, S.E., et al., 2022. An overview of GPR subsurface exploration of planets and moons. Lead. Edge 41 (10), 672–680. https://doi.org/10.1190/tle41100672.1.

Pieters, C., Mcfadden, L., 2003. Meteorite and asteroid reflectance spectroscopy: clues to early solar system processes. Annu. Rev. Earth Planet. Sci. 22, 457–497. https://doi.org/10.1146/annurev.ea.22.050194.002325.

Radon, J., 1986. On the determination of functions from their integral values along certain manifolds. IEEE Trans. Med. Imaging 5 (4), 170–176. https://doi.org/10.1109/TMI.1986.4307775.

Raducan, S.D., Jutzi, M., Cheng, A.F., et al., 2024. Physical properties of asteroid dimorphos as derived from the dart impact. Nature Astronomy 8 (4), 445–455. https://doi.org/10.1038/s41550-024-02200-3.

Richardson, J.E., Melosh, H.J., Greenberg, R.J. et al. (2005). The global effects of impact-induced seismic activity on fractured asteroid surface morphology. Icarus, 179(2), 325–349. URL: https://www.sciencedirect.com/science/article/pii/S0019103505002472. doi:10.1016/j.icarus.2005.07.005.

Rosen, P., Hensley, S., Joughin, I., et al., 2000. Synthetic aperture radar interferometry. Proc. IEEE 88 (3), 333–382. https://doi.org/10.1109/5.838084.

Rothberg, S., Allen, M., Castellini, P. et al. (2017). An international review of laser Doppler vibrometry: Making light work of vibration measurement. Optics and Lasers in Engineering, 99, 11–22. URL: https://www.sciencedirect.com/science/article/pii/S0143816616303724. doi:10.1016/j.optlaseng.2016.10.023.

Roy, R., Kailath, T., 1989. Esprit-estimation of signal parameters via rotational invariance techniques. IEEE Trans. Acoust. Speech Signal Process. 37 (7), 984–995. https://doi.org/10.1109/29.32276.

Ruigrok, E., Draganov, D., & Wapenaar, K. (2008). Global-scale seismic interferometry: theory and numerical examples. Geophysical Prospecting, 56(3), 395–417. URL: https://onlinelibrary.wiley.com/doi/abs/10.1111/j.1365-2478.2008.00697.x. doi: 10.1111/j.1365-2478.2008.00697.x.

Satpathy, A., Mainzer, A., Masiero, J.R., et al., 2022. Neowise observations of the potentially hazardous asteroid (99942) apophis. Planet. Sci. J. 3 (5), 124. https://doi.org/10.3847/PSJ/ac66d1.

Sava, P., Asphaug, E., 2019. Seismology on small planetary bodies by orbital laser doppler vibrometry. Adv. Space Res. 64 (2), 527–544. https://doi.org/10.1016/j.asr.2019.04.017.

Sava, P.C., Fomel, S., 2003. Angle-domain common-image gathers by wavefield continuation methods. Geophysics 68 (3), 1065–1074. https://doi.org/10.1190/1.1581078.

Scheeres, D., Hartzell, C., Sánchez, P. et al. (2010). Scaling forces to asteroid surfaces: The role of cohesion. Icarus, 210(2), 968–984. URL: https://www.sciencedirect.com/science/article/pii/S0019103510002812. doi: 10.1016/j.icarus.2010.07.009.

Schmidt, R.O., 1986. Multiple emitter location and signal parameter estimation. IEEE Trans. Antennas Propag. 34 (3), 276–280. https://doi.org/10.1109/TAP.1986.1143830.

Spencer, J.R., Stern, S.A., Moore, J.M., et al., 2020. The geology and geophysics of kuiper belt object (486958) arrokoth. Science 367 (6481). https://doi.org/10.1126/science.aay3999, URL: https://www.science.org/doi/abs/10.1126/science.aay3999. arXiv:https://www.science.org/-doi/pdf/10.1126/science.aay3999.

Spetzler, J., Snieder, R., 2004. The Fresnel volume and transmitted waves. Geophysics 69, 653–663. https://doi.org/10.1190/1.1759451.

Stickle, A.M., DeCoster, M.E., Burger, C., et al., 2022. Effects of impact and target parameters on the results of a kinetic impactor: Predictions for the double asteroid redirection test (dart) mission. The. Planet. Sci. J. 3 (11), 248. https://doi.org/10.3847/PSJ/ac91cc.

Walsh, K., Jawin, E.R., Ballouz, R.L. et al. (2019). Craters, boulders and regolith of (101955) bennu indicative of an old and dynamic surface. Nature Geoscience, 12(4), 242–246. URL: https://ui.adsabs.harvard.edu/abs/2019NatGe.12.242W. doi:10.1038/s41561-019-0326-6.

Wapenaar, K., Brackenhoff, J., Thorbecke, J., 2019. Green's theorem in seismic imaging across the scales. Solid Earth 10, 517–536. https://doi.org/10.5194/se-10-517-2019, URL: https://se.copernicus.org/articles/10/517/2019/.

Wapenaar, K., Draganov, D., Snieder, R., et al., 2010. Tutorial on seismic interferometry: Part 1 - Basic principles and applications. Geophysics 75 (5). https://doi.org/10.1190/1.3457445.

Watkins, J.S., Kovach, R.L., 1973. Seismic investigation of the lunar regolith. Lunar Planet. Sci. Conf. Proc. 4, 2561.

Zelt, C.A., Smith, R.B., 1992. Seismic traveltime inversion for 2-D crustal velocity structure. Geophys. J. Int. 108 (1), 16–34. https://doi.org/10.1111/j.1365-246X.1992.tb00836.x.